Journal of Power Sources 668 (2026) 239365

Contents lists available at ScienceDirect

Journal of Power Sources

journal homepage: www.elsevier.com/locate/jpowsour

Cost-effective sodium-ion batteries using a $Na_{0.67}Mn_{0.9}Ni_{0.1}O_2$ cathode and lavender-flower-waste-derived hard carbon with a comparative presodiation approach

Ebru Dogan [a,1], Iqra Moeez [b,1], Rawdah Whba [a,c], Sibel Ozcan [d], Mitat Akkoc [e], Emine Altin [f], Messaoud Harfouche [g], Aydin Aktas [f], Fatih Bulut [a], Muhammad Arshad [h], Ismail Ozdemir [i], Saban Patat [j], Kyung Yoon Chung [b,k,*], Sevda Sahinbay [l,**], Serdar Altin [a,***]

[a] Physics Department, Inonu University, Malatya, 44280, Türkiye
[b] Energy Storage Research Center, Korea Institute of Science and Technology, Seongbuk-gu, Seoul, 02792, Republic of Korea
[c] Department of Chemistry, Faculty of Applied Sciences, Taiz University, Taiz, 6803, Yemen
[d] Department of Physics, Aksaray University, Aksaray, 68100, Türkiye
[e] Hekimhan Mehmet Emin Sungur Vocational School, Malatya Turgut Ozal University, Malatya, 44400, Türkiye
[f] Vocational School of Health Service, Inonu University, Battalgazi, Malatya, 44280, Türkiye
[g] Synchrotron-light for Experimental Science and Applications in the Middle East (SESAME), Allan, 19252, Jordan
[h] Nano-sciences & Technology Department, National Centre for Physics (NCP), Quaid-i-Azam University (QAU) Campus, Islamabad, 44000, Pakistan
[i] Chemistry Department, Inonu University, Malatya, 44280, Türkiye
[j] Chemistry Department, Erciyes University, Kayseri, 38260, Türkiye
[k] Division of Energy and Environment Technology, KIST School, Korea University of Science and Technology, Seoul, 02792, Republic of Korea
[l] Physics Engineering Department, Istanbul Technical University, Istanbul, 34475, Türkiye

HIGHLIGHTS

- Cost-effective, high-performance sodium-ion batteries (SIBs) are desired.
- We fabricate low-cost SIBs and investigate presodiation methods.
- The electrodes use accessible precursors, ensuring scalability and sustainability.
- Direct contact presodiation provides the highest initial full-cell capacity.
- Electrochemical presodiation provides superior cycling stability and energy density.

GRAPHICAL ABSTRACT

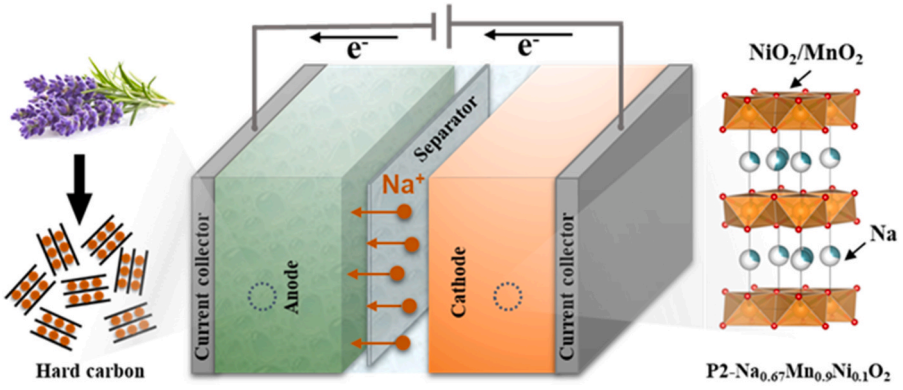

* Corresponding author. Energy Storage Research Center, Korea Institute of Science and Technology, Seongbuk-gu, Seoul, 02792, Republic of Korea.
** Corresponding author.
*** Corresponding author.
E-mail addresses: kychung@kist.re.kr (K.Y. Chung), sevdasahinbay25@gmail.com (S. Sahinbay), serdar.altin@inonu.edu.tr (S. Altin).
[1] These authors contributed equally.

https://doi.org/10.1016/j.jpowsour.2026.239365
Received 20 July 2025; Received in revised form 12 January 2026; Accepted 15 January 2026
Available online 23 January 2026

ARTICLE INFO

Keywords:
Na-ion cell
P2-type cathode
Lavender flowers
In situ synchrotron X-ray absorption fine structure
Presodiation

ABSTRACT

The development of cost-effective, high-performance sodium-ion batteries (SIBs) is essential for large-scale energy storage systems. In this study, low-cost SIBs are fabricated using P2-type $Na_{0.67}Mn_{0.9}Ni_{0.1}O_2$ as the cathode and hard carbon (HC) derived from lavender flower waste as the anode. The synthesis of both electrode materials from widely accessible precursors ensures scalability and environmental sustainability. To address the sodium deficiency of HC, three different presodiation strategies—electrochemical, chemical, and direct contact—are systematically investigated, and the electrochemical performances of the full cells are compared. This evaluation reveals significant variations in the initial capacity, capacity retention, Coulombic efficiency, and rate performance. Although the direct-contact method delivers the highest initial capacity, electrochemical presodiation delivers superior long-term cycling stability and enhanced energy density. This comprehensive comparison of the electrochemical performance emphasizes the vital role of presodiation in enhancing the full-cell efficiency, while highlighting the potential methods for developing cost-effective and sustainable SIBs.

1. Introduction

Current energy storage solutions are significantly dependent on rechargeable batteries, powering a wide range of applications from portable devices to electric vehicles and large-scale stationary energy storage systems [1,2]. Sodium-ion batteries (SIBs), the predominant technology used in these applications, are gaining attention as viable and sustainable alternatives to lithium-ion batteries (LIBs) because of the abundance of sodium [3,4]. In particular, the manufacturing process of SIBs closely resembles that of LIBs, enabling their straightforward integration into existing production systems [5–7]. Their compatibility and potential to replace LIBs may reduce production costs by 10–20 %, thereby improving the capacity of electrode materials to meet the growing demand for cost-effective and eco-friendly energy solutions [8].

Among the various promising cathode materials for SIBs, P2-type layered cathode materials with stoichiometric $Na_{0.67}MnO_2$ have been widely studied primarily because of their cost-effectiveness, structural stability, fast diffusion kinetics, and excellent rate capability [9–14]. However, despite good mobility of sodium, undesirable properties such as multiple phase transitions, Jahn–Teller (JT) distortions of Mn^{3+} ions, and irreversible anion redox reactions lead to fast capacity decay and insufficient cycling stability [15–17]. To mitigate this intrinsically poor cycling stability, partial substitution of metals such as Ti, Li, Mg, Cu, W and Al in $Na_{0.67}MnO_2$ has been investigated [18–23]. Substituents with valence states lower than 3+ increase the proportion of Mn^{4+} ions in the structure, thereby reducing the number of JT-active Mn^{3+} ions. As the size of Ni^{2+} (0.69 Å) is comparable to that of Mn^{3+} (0.645 Å), it is possible to substitute Ni in $Na_{0.67}MnO_2$ to form $Na_{0.67}Mn_{1-x}Ni_xO_2$. This Ni substitution not only enhances the structural stability during cycling by suppressing the JT effect associated with Mn^{3+} ions but also elevates the average electrode potential via the Ni^{4+}/Ni^{2+} redox couple, resulting in an enhanced specific capacity [24,25]. Therefore, $Na_{0.67}Mn_{1-x}Ni_xO_2$ has been extensively applied as a layered transition metal oxide. For example, $Na_{0.67}Ni_{0.15}Mn_{0.85}O_2$ has demonstrated a capacity of 101 mAh/g after 120 cycles at 100 mA/g within a 2.0–4.3 V window, retaining 96.8 % of its capacity [26]. Furthermore, Xiao et al. reported that an optimum Mn/Ni ratio of 0.9/0.1 in $Na_{0.8}Mn_{1-x}Ni_xO_2$ (x = 0.0, 0.1, 0.2, 0.3) achieved superior SIB performance [27]. Beyond their electrochemical advantages, their high abundance and low production costs make Mn and Ni promising elements for use in commercial SIBs.

Hard carbon (HC) is the most used anode material in SIBs and is characterized by a disordered carbon structure. HC provides multiple benefits, such as a high capacity, extended cycle life, and outstanding rate capability, making it a highly promising option for use in batteries. Various organic precursors such as phenolic resins, polyacrylonitrile (PAN), and cellulose have been employed for HC production [28–30]. The production methods for HC include pyrolysis, carbonization, and chemical vapor deposition, utilizing raw materials such as graphite waste, coal tar, and biomass [28–32]. In recent years, scientists have focused on new bio-sources for HC production, such as rice husks, corn stover, wheat straw, olive pits, apricot seeds, and coconut shells, and the specific capacity of HC varies from 200 to 400 mAh/g depending on the source materials [33–35].

Plant diversity and production capacity are important factors affecting the commercialization of SIBs, as plant-derived HCs are both sustainable and economical. HC derived from plants preserves the microstructures of the plant tissues, thereby enhancing the penetration of the electrolyte and sodium diffusivity. Lignocellulose wastes not only provide an opportunity for obtaining economical materials but also address agricultural residue management while reducing CO_2 emissions due to carbonization [36]. For example, lavender production, a prominent and growing sector renowned for its high-quality essential oils and dried flowers, is estimated at approximately 1000–1500 tons annually. After the extraction of the lavender essential oil, a substantial amount of lavender flower waste remains [37]. This waste can be repurposed for HC production, providing a high-value product by using it as a raw material for HC. However, the use of lavender flowers as an anode material in SIBs has not been adequately investigated.

Generally, P2-type cathode material and hard carbon anode material are promising electrodes for full-cell performance. Although, in half cells, sodium metal acts as a continuous source to replenish the consumed sodium ions in the formation of the solid-electrolyte interphase (SEI) layer. However, the hard carbon anode and P2-type cathode material in the full cell have insufficient sodium reservoirs, resulting in poor electrochemical performance. Several strategies have been studied to address this challenge. For example, the coated P2-$Na_{0.67}Mn_{0.5}Fe_{0.5}O_2$ coupled with presodiated hard carbon by direct method shows enhanced cycling stability and improved capacity retention in sodium-ion full cells with better interfacial stabilization and sodium balancing at the full-cell level [38,39]. Similarly, Wu et al. conducted electrochemical presodiation of hard carbon in a half cell and afterward fabricated a full cell using presodiated hard carbon and a P2-$Na_{0.67}Mn_{0.33}Ni_{0.33}Fe_{0.33}O_2$ cathode [40]. Qian et al. treated the hard carbon by immersing it in the sodium-based solution and forming a presodiated hard carbon, resulting in a high initial Coulombic efficiency of ~95 % in a full cell coupled with $Na_3V_2(PO_4)_3$ [41]. Despite these advances, systematic comparisons of electrochemical, chemical, and direct-contact presodiation strategies within the same P2-type layered oxide and biomass-derived hard carbon full-cell system remain limited. The present work addresses this gap by evaluating the full-cell performance of P2-$Na_{0.67}Mn_{0.9}Ni_{0.1}O_2$ coupled with lavender flower waste-derived hard carbon under different presodiation approaches.

In this study, P2-type $Na_{0.67}Ni_{0.1}Mn_{0.9}O_2$ was synthesized as a cathode material using a conventional solid-state method, and the anode material was innovatively fabricated from lavender flowers acquired from local markets, Türkiye. The structural properties of both electrodes were thoroughly characterized using common techniques including X-ray diffraction (XRD), scanning electron microscopy (SEM), X-ray photoelectron spectroscopy (XPS), Fourier-transform infrared

spectroscopy (FTIR), and Raman spectroscopy, as well as unconventional methods such as in situ synchrotron X-ray absorption fine structure (XAFS) spectroscopy to track real-time structural and electronic changes. Furthermore, their electronic properties were determined by density functional theory (DFT) calculations. The electrochemical properties of both electrodes were evaluated using half- and full-cell tests with three different presodiation techniques involving chemical, electrochemical, and direct-contact methods, and their relative performances are comprehensively assessed.

2. Results and discussion

2.1. Structural properties of the electrodes

The cathode and anode powders were initially characterized by XRD analysis, as shown in Fig. 1a and b, respectively. The crystal structure of the $Na_{0.67}Ni_{0.1}Mn_{0.9}O_2$ cathode was examined using Rietveld refinement (Fig. S1), revealing *P6₃/mmc* hexagonal symmetry with lattice parameters of a = 2.88398(2) Å, c = 11.20949(3) Å, and a volume of 80.776(4) Å^3. These values are consistent with those obtained from neutron diffraction studies (a = 2.87161 Å and c = 11.18154 Å) [42,43]. The XRD pattern of the HC-based lavender flowers is displayed in Fig. 1b, showing two broad peaks at 22.5° (002) and 43.07° (100), which are characteristic of HC. In addition, SEM was used to analyze the morphologies of both samples, as depicted in Fig. 1c. The $Na_{0.67}Ni_{0.1}Mn_{0.9}O_2$ sample had a grain size of approximately 1–3 μm, while the HC sample displayed a porous surface structure. The TEM images and EDS elemental mapping of $Na_{0.67}Ni_{0.1}Mn_{0.9}O_2$ are shown in Fig. 1d and Fig. S2, respectively. The SAED pattern (Fig. S2) confirms the crystalline nature of the material, while the EDS elemental mapping (Fig. 1d) reveals a homogenous distribution of Ni atoms throughout the structure.

The valence states and elemental composition of $Na_{0.67}Ni_{0.1}Mn_{0.9}O_2$ were further investigated using XPS. The Mn 2p, Ni 2p, Na 1s, and O 1s peaks are shown in Fig. 1e and Fig. S3. In the Mn 2p XPS spectrum (Fig. 1e), the binding energy peaks for Mn $2p_{3/2}$ and Mn $2p_{1/2}$ are located at 643.1 and 654.8 eV, respectively [44,45]. The fitting results for Mn indicate the presence of Mn^{3+} and Mn^{4+} in Mn $2p_{3/2}$ and Mn $2p_{1/2}$. Based on these peak areas, the peak ratio of Mn^{3+}/Mn^{4+} is 0.52, suggesting a reduction in Mn^{3+} after Ni doping. This reduced content of Mn^{3+} with an average valence state of Mn from +3.33 to +3.66 suppresses phase transitions driven by undesirable JT distortion, thereby improving structural stability. As shown in the Ni 2p XPS spectrum (Fig. 1e), the peaks at approximately 855.5 and 872.8 eV are related to Ni^{2+}, while those at 856.6 and 873.9 eV correspond to Ni^{3+} [44,45], with two satellite peaks at 861.8 and 879.3 eV. The Ni^{2+}/Ni^{3+} ratio in $Na_{0.67}Ni_{0.1}Mn_{0.9}O_2$ determined from the peak areas is 0.61 with an average valence state of +2.62. Therefore, the average valence state of the transition metals is +3.55, which is higher than the expected value of +3.33, thereby exhibiting enhanced structural stability.

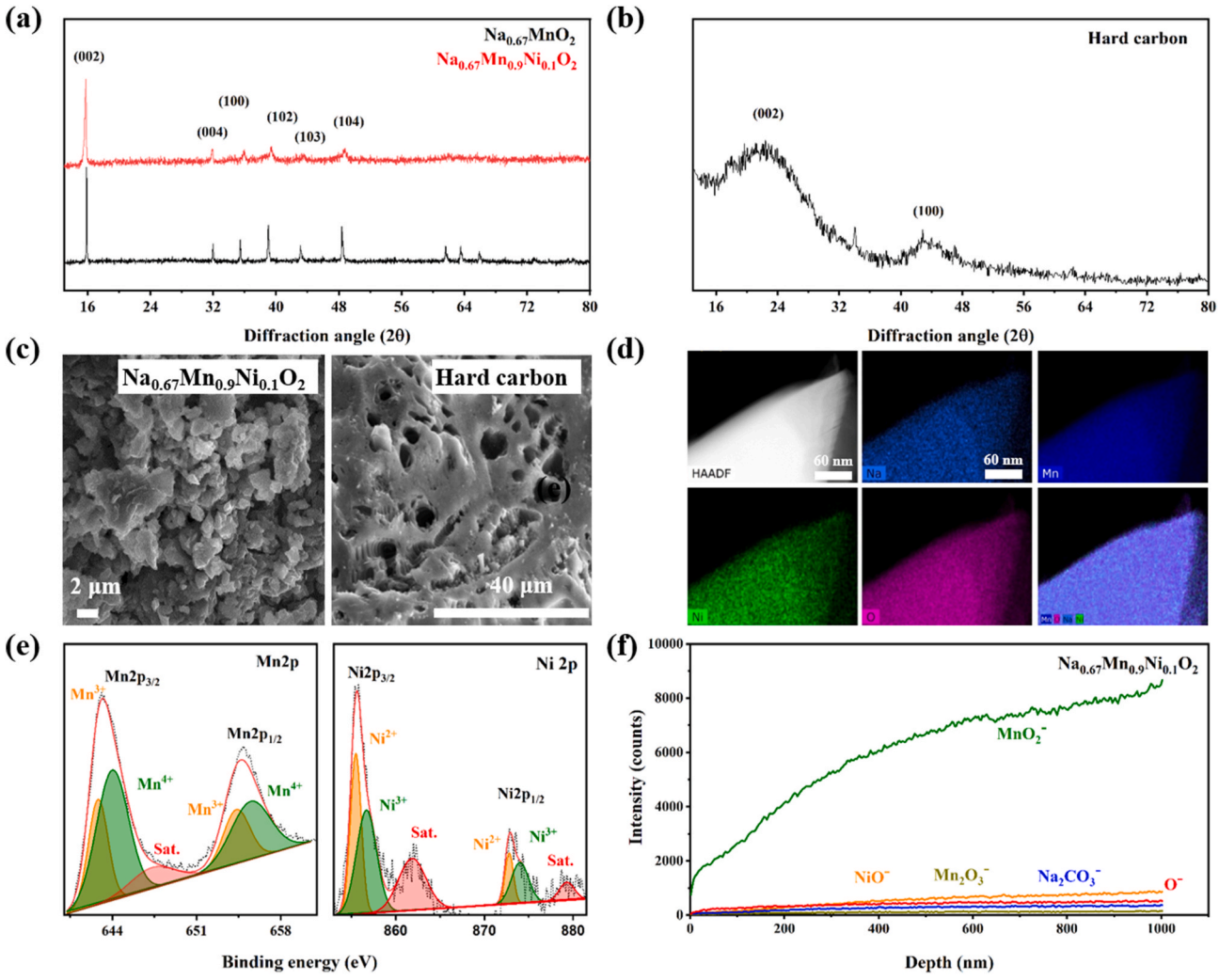

Fig. 1. XRD patterns of (a) $Na_{0.67}Ni_{0.1}Mn_{0.9}O_2$ and (b) lavender flower-based HC, respectively. (c) SEM images of the cathode and anode materials. (d) TEM image with EDS element mapping, (e) Mn 2p and Ni 2p XPS spectra, and (f) TOF-SIMS depth profiles of $Na_{0.67}Ni_{0.1}Mn_{0.9}O_2$.

The TOF-SIMS profiles and 3D distributions of the $Na_2CO_3^-$, $Mn_2O_3^-$, MnO_2^-, NiO^-, and O^- ions are shown in Fig. 1f and Fig. S4. The concentrations of these ions increased as the sputtering depth increased. The distribution of these species was visualized via 3D images, as shown in Fig. S4. The signals from MnO_2^- and NiO^- are consistent with the XPS results, indicating an increase in Mn^{4+} after the homogenous incorporation of Ni within the structure.

The integration of Ni within the $Na_{0.67}MnO_2$ crystal structure was further confirmed by the appearance of vibration peaks in the FTIR (Fig. S5) and Raman (Fig. S6) spectra. BET analyses (Fig. S7) were performed to investigate HC, and the surface area, micro-pore volume, and average pore size were measured as 3.3 m^2/g, 0.007 cm^3/g, and 6.2 Å, respectively.

The electronic properties were analyzed using DFT calculations. Self-consistent solutions were achieved using a (15 × 5 × 3) gamma grid of k-points for integration over the Brillouin zone, applied to the 1 × 5 × 1 supercells of $Na_{0.67}MnO_2$ and $Na_{0.67}Ni_{0.1}Mn_{0.9}O_2$, as shown in Fig. 2a and b, respectively. The Perdew–Burke–Ernzerhof parameterization treats exchange-correlation effects with additional Hubbard-U correction terms. The Hubbard-U values for Mn and Ni atoms were set as 4.95 and 6.30 eV, respectively [46,47]. The lattice constants and atomic positions were thoroughly refined, and all the force components were smaller than 0.01 eV $Å^{-1}$. The calculated lattice parameters were a = 3.22 and 2.96 Å for $Na_{0.67}MnO_2$ and $Na_{0.67}Ni_{0.1}Mn_{0.9}O_2$, respectively. As the Hubbard-U parameter increased, the localization of 3d electrons was enhanced, thereby increasing the lattice parameters [48]. The most stable configuration was determined by calculating the formation energy using the following equation:

$$\Delta H = E_{Na_xMn_{1-y}Ni_yO_2} - (1-x)E_{Mn_{1-y}Ni_yO_2} - xE_{NaMn_{1-y}Ni_yO_2} \quad (1)$$

where E refers to the total energy of the most stable structures of the $Na_xMn_{1-y}Ni_yO_2$, $Mn_{1-y}Ni_yO_2$, and $NaMn_{1-y}Ni_yO_2$, respectively. The negative formation energies of $Na_{0.67}MnO_2$ (−0.1 eV/f.u.) and $Na_{0.67}Ni_{0.1}Mn_{0.9}O_2$ (−0.43 eV/f.u.) indicate that the synthesis of these structures is highly feasible.

The effect of Ni doping on the electronic structure of $Na_{0.67}MnO_2$ was studied using DFT calculations. As shown in Fig. 2c and d, the $Na_{0.67}MnO_2$ and $Na_{0.67}Ni_{0.1}Mn_{0.9}O_2$ exhibited metallic characteristics. Below the Fermi level, the total and partial DOS, which are primarily dominated by the Mn (d) and O (p) states, respectively, showed no significant differences. After Ni doping, the bandgap between 0.1 and 2.4 eV (Fig. 2d) became almost negligible, indicating enhanced electronic conductivity in the material. This observation aligns with similar findings for Co-doped P2-$Na_{0.67}MnO_2$ [48]. To explore the magnetic properties of $Na_{0.67}MnO_2$ and $Na_{0.67}Ni_{0.1}Mn_{0.9}O_2$, the total energies of the ferromagnetic (FM), nonmagnetic (NM), and antiferromagnetic (AFM) spin configurations were calculated, as summarized in Table S1. The FM and AFM configurations are shown in Fig. 2e and f. As shown in Table S1, $Na_{0.67}MnO_2$ adopts an AFM configuration with a supercell magnetic moment of 2.00 μ_B. The ground state of $Na_{0.67}Ni_{0.1}Mn_{0.9}O_2$ was determined to be FM, with a supercell magnetic moment of 8.46 μ_B. The magnetic moment predominantly originates from the Mn and Ni atoms because the contributions from the O and Na atoms are negligible. The spin-dependent electronic band structures of $Na_{0.67}MnO_2$ (AFM) and $Na_{0.67}Ni_{0.1}Mn_{0.9}O_2$ (FM) are shown in Fig. 2g and h, respectively. Remarkably, the band structure of $Na_{0.67}MnO_2$ exhibits semiconducting behavior with an energy gap of 2.50 eV. By contrast, $Na_{0.67}Ni_{0.1}Mn_{0.9}O_2$ exhibits metallic behavior. These findings align with those of previous calculations for $Na_{0.67}MnO_2$ with a reported energy gap of 2.21 eV [48,49]. In addition, experimental studies have indicated that the $NaMnO_2$ structure exhibits an AFM structure near 0 K [48,49].

2.2. Half-cell electrochemical properties

Fig. 3a and b illustrate the capacity-voltage curves for the 1st, 10th, 25th, 50th, 75th, and 100th cycles of $Na_{0.67}Ni_{0.1}Mn_{0.9}O_2$ and HC, measured within the voltage windows of 1.5–4.3 and 0.0–3.0 V, respectively. The initial charge and discharge capacities of the electrodes were 201 and 200 mAh/g for $Na_{0.67}Ni_{0.1}Mn_{0.9}O_2$ and 260 and 360 mAh/g for HC, respectively, with columbic efficiencies of 99.5 % and 72 %. After 100 cycles, these values decreased to 83 and 243 mAh/g, respectively, corresponding to respective capacity retention rates of 42 % and 67.4 % (Fig. 3c). The C-rate performance of both electrodes in

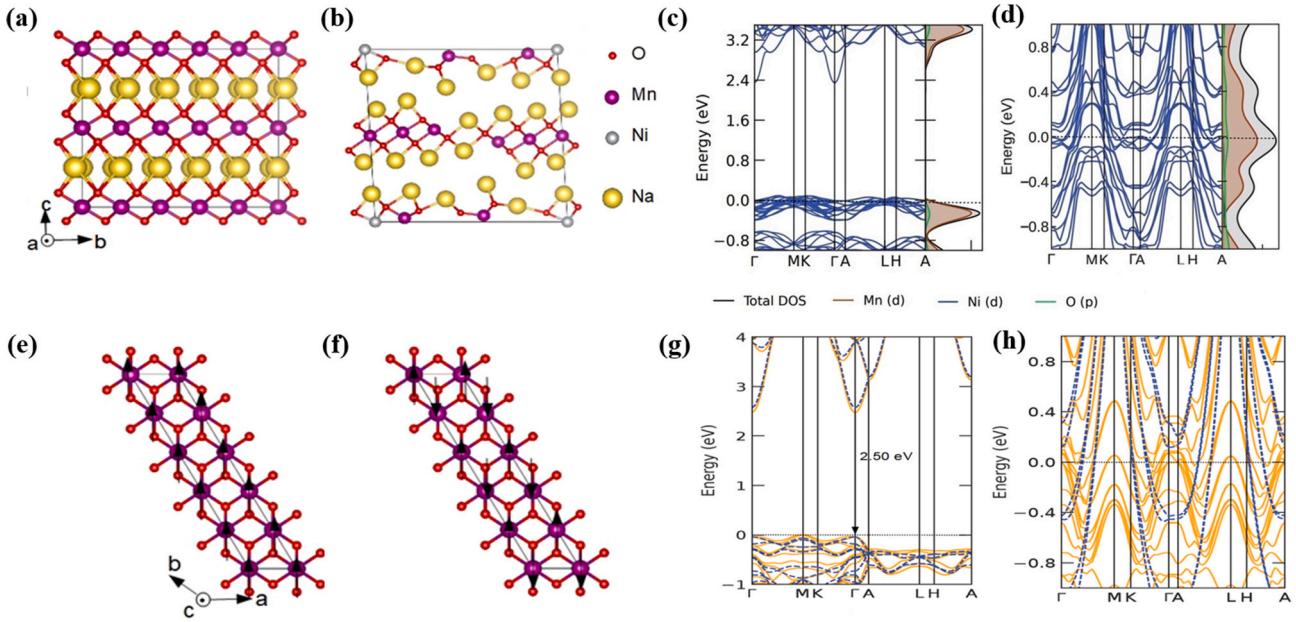

Fig. 2. Side views of (a) $Na_{0.67}MnO_2$ and (b) $Na_{0.67}Ni_{0.1}Mn_{0.9}O_2$. Band structure (left panel) and partial density of states (PDOS) (right panel) of (c) $Na_{0.67}MnO_2$ and (d) $Na_{0.67}Ni_{0.1}Mn_{0.9}O_2$. The dashed line indicates the Fermi level. Top views of $Na_{0.67}MnO_2$ showing the (e) ferromagnetic (FM) and (f) antiferromagnetic (AFM) states. Spin-resolved band structures of (g) $Na_{0.67}MnO_2$ and (h) $Na_{0.67}Ni_{0.1}Mn_{0.9}O_2$. The spin-up and -down bands are represented by solid orange and dotted blue lines, respectively. The Fermi level was fixed at 0 eV. The black arrow shows the fundamental bandgap. (For interpretation of the references to colour in this figure legend, the reader is referred to the Web version of this article.)

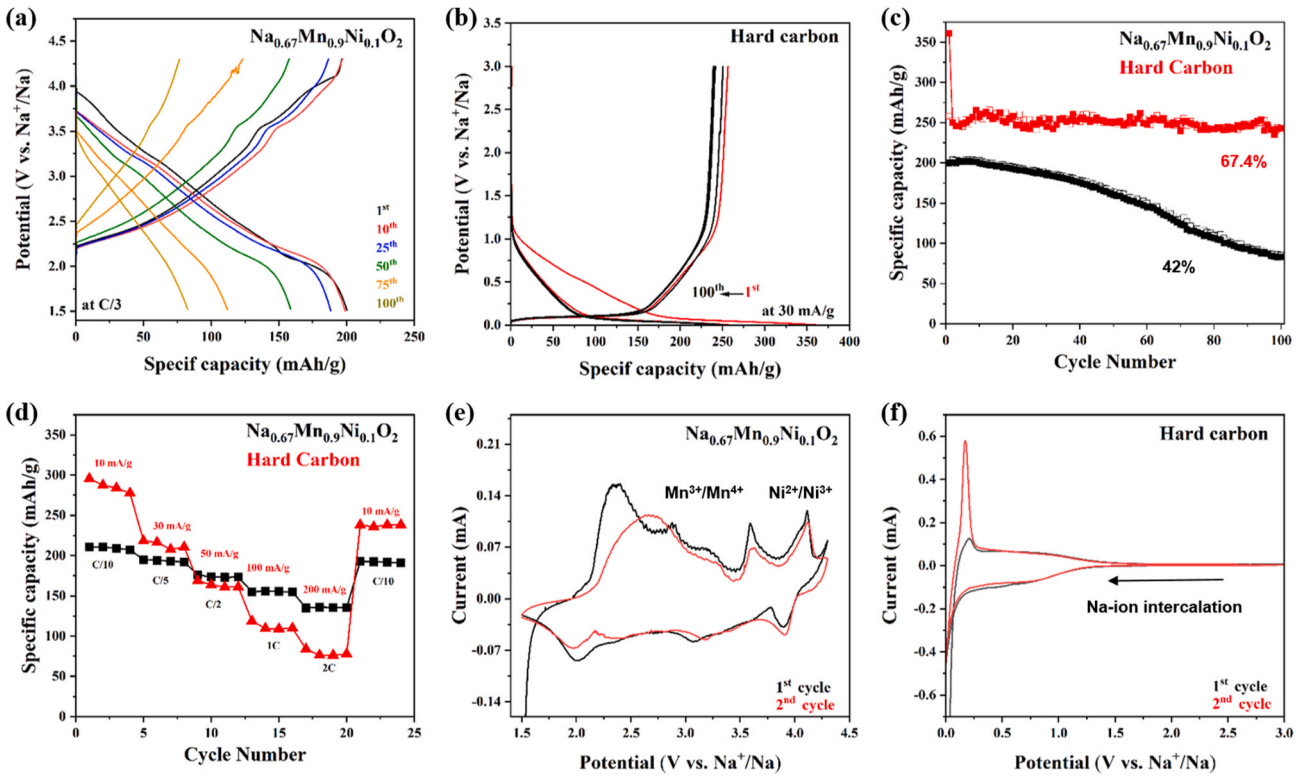

Fig. 3. Voltage–capacity graphs of (a) $Na_{0.67}Ni_{0.1}Mn_{0.9}O_2$ and (b) HC half cells. (c) Capacity retention of the cathode and anode materials at C-rates of C/3 and 30 mA/g, respectively, along with their (d) C-rate performance. CV profiles of (e) $Na_{0.67}Ni_{0.1}Mn_{0.9}O_2$ and (f) HC.

the half-cell configuration is shown in Fig. 3d. For $Na_{0.67}Ni_{0.1}Mn_{0.9}O_2$ and HC, the capacities decreased from 209 and 298 mAh/g at a C/10-rate (10 mA/g) to 122 and 84 mAh/g at a 2C-rate (200 mA/g), respectively. Table S2 summarizes previously reported results for similar cathodes and HCs, demonstrating that our findings are in good agreement with the literature. Particularly, for the HC, in the sloping region >1.0 V, Na^+ ions are adsorbed onto defect sites, edges, and functional groups on the carbon surface. However, at lower potentials (below ~0.1 V), Na^+ storage is dominated by the filling of internal closed pores or nanopores within the turbostratic carbon structure, giving rise to the characteristic plateau behavior. This pore-filling mechanism is diffusion-controlled and is strongly dependent on the type, size, and distribution of micropores. The interplay between these two mechanisms governs the overall reversible capacity and initial coulombic efficiency of hard carbon [50].

Furthermore, CV measurements were conducted to determine the half-cell electrochemical properties of the cathode, using Na metal as the counter electrode within the voltage window of 1.5–4.3 V (vs. Na^+/Na) at a scan rate of 0.1 mV/s (Fig. 3e). In the first cycle (Fig. 3e), five different redox peaks were observed at 2.35, 2.88, 3.23, 3.59, and 4.12 V during the charging process, which correspond to Mn^{3+}/Mn^{4+} redox transitions, Na-ion ordering, and the oxidation of Ni^{2+} to Ni^{3+} [45]. High-voltage peaks indicate the electrolyte oxidation and formation of a cathode electrolyte interface. Fig. 3f shows the CV curve for HC within a voltage window of 0.0–3.0 V (vs. Na^+/Na) at a scan rate of 0.1 mV/s [50]. The single redox peak observed at 0.17 V is characteristic of the intercalation and de-intercalation of sodium ions in HC. In addition, GITT analysis (Fig. S8) was performed, which is a powerful technique for determining the dynamic diffusion coefficient during the charge and discharge processes. The observed D_{Na}^+ values for both the cathode and anode confirm that they exhibited fastest sodium diffusion kinetics compared to previously published electrodes. It is worth noting that a good full-cell performance necessitates comparable D_{Na}^+ values for both the anode and cathode, and a high D_{Na}^+ is indicative of a high specific capacity [51], as observed in our measurements and further confirmed through EIS analyses (Fig. S9 and Table S3).

2.3. *In situ XAFS and XRD experiments*

In situ XANES measurements were performed using a CR2032 coin cell, and the normalized XAFS plots for the Mn and Ni K-edges during cycling are shown in Fig. 4a and b, respectively. It is evident that Mn exhibited a clear shift to higher energies during charging. Mn is predominantly present as Mn^{4+} in $Na_{0.67}Ni_{0.1}Mn_{0.9}O_2$, as discussed in the XPS analysis (Fig. 1). During the charge process up to 4.3 V (green line), a noticeable shift in the Mn K-edge XANES spectra was observed from 6559.8 eV at the open circuit voltage to 6561.1 eV, suggesting the oxidation of Mn^{3+} to Mn^{4+} in the fully charged state (Fig. 4a). Upon subsequent discharging to 1.5 V (inset of Fig. 4a), the shape of the Mn K-edge returned (red line), suggesting the complete reduction of Mn^{4+} to Mn^{3+} [38,52]. Meanwhile, the Ni K-edge of the pristine material suggests an initial oxidation state of $Ni^{2.5+}$, which is in agreement with the XPS results. The signal shifted to higher energy, corresponding to oxidation from the Ni^{2+} and Ni^{3+} states during cycling (Fig. 4b), reflecting a contribution to the specific charge capacity along with Mn. However, during discharge to 1.5 V (inset of Fig. 4a), the Ni K-edge energy shifted to a lower energy (red line), which is consistent with a previous report [53]. Overall, these results suggest a reversible change in the Mn and Ni oxidation states during charging and discharging.

Furthermore, the local structure around the Mn and Ni ions was determined using the Fourier transform of the EXAFS signal. The resulting contour plots are shown in Fig. 4c. The first and second peaks denote the metal–oxygen (Mn/Ni-O) and metal–metal (M-M, M = Mn, Ni) bonds, respectively [54]. The changes in the interatomic distances of Mn-O (1.41 Å) and Ni-O (1.62 Å) at the Mn and Ni K-edges confirm the Mn and Ni redox reactions, respectively. When the cathode was fully charged to 4.3 V, the intensities and bond distances of Mn-O and Ni-O decreased, indicating their oxidation to higher oxidation states [54].

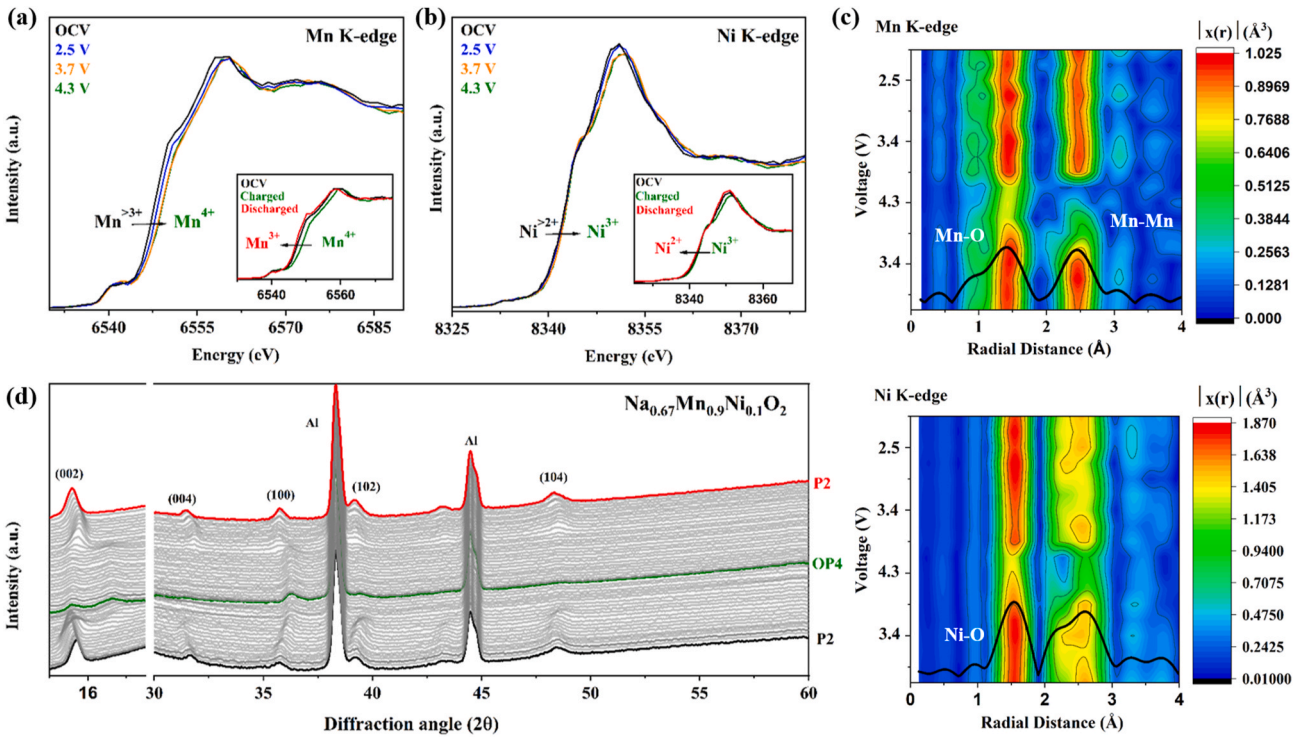

Fig. 4. In situ XANES data obtained at different voltages and collected for the (a) Mn and (b) Ni K-edge. Contour plots of the Fourier-transformed EXAFS signal analysis of the (c) Mn and Ni K-edge. (d) In situ XRD pattern for $Na_{0.67}Ni_{0.1}Mn_{0.9}O_2$ measured within a voltage window of 1.5–4.3 V at a 0.1C-rate.

Afterward, the M − O distance and intensity increased again during the discharge process. Similar changes were observed in the Mn - Mn (2.46 Å) inter-atomic distances during the charging/discharging processes, confirming a reversible change in the structure during cycling.

The in situ XRD patterns (Fig. 4d) show structural changes in $Na_{0.67}Ni_{0.1}Mn_{0.9}O_2$ during the initial cycle. The peaks in the XRD pattern of the pristine electrode (black line) confirm the P2 phase of the layered oxide material. During charging, the peaks at $2\theta = 15.8°$, 31.5°, 39.5, and 48.5° began to decrease, indicating the disappearance of the P2 phase due to a change in the long-range order. In the XRD pattern of the fully charged electrode (green line), a new peak appeared at $2\theta = 17°$, indicating the presence of a new OP4 phase at high voltages [53]. The in situ XRD patterns during the discharge process confirmed that this P2-OP4 phase transition was reversible, where the peaks related to OP4 disappeared, and the P2 phase reflexes became stronger until the end of the discharge process (red line).

2.4. Full-cell electrochemical properties

A critical step in the commercialization of SIBs is a performance-based evaluation through full-cell tests. Typically, the formation and aging of full cells are key challenges that are closely guarded as proprietary knowledge by companies. Most importantly, the formation of a solid electrolyte interface (SEI) layer is a sodium-consuming process that limits battery performance [38,41,55]. An approach to address SEI layer formation involves the presodiation process, which can effectively improve the full-cell performance. It has been observed that the presodiation process compensates for sodium loss, contributes to the integrity of the SEI, and leads to better electrochemical performance. There are three types of presodiation strategies for anode materials: (i) DCP, (ii) ECP, and (iii) CP; detailed descriptions are available in **Note S1**. Although all presodiation strategies for anode materials promote stable SEI formation, a comparative study can provide further insight into the advantages of each process. In this study, a full-cell performance analysis was conducted using different presodiation methods, as outlined in the experimental section.

Galvanostatic cycling tests were performed with five cycles at a C/10-rate for formation and 200 cycles at a C/2-rate. The capacity–voltage profiles of the full cells using the DCP, ECP, and CP anodes are shown in Fig. 5a–c. The initial charge capacities at the C/10-rate were 211, 114, and 102 mAh/g, with discharge capacities of 201, 108, and 98 mAh/g for DCP, CP, and ECP, respectively, showing a Coulombic efficiency of 95.2 %, 94.7 % and 96 % after the 1st cycle. A detailed comparison of the cyclic performances after 200 cycles at a C/2 rate is shown in Fig. 5d. A comparative study of the three full cells showed capacity retentions of 56 %, 29.7 %, and 62 % for the DCP, CP, and ECP methods, respectively. The DCP method delivered the highest initial capacity, while the ECP method provided the best capacity retention. The loss of capacity in DCP method could be due to the uncontrolled reactions between electrolyte and sodium metal, leading to a thick and non-uniform formation of an SEI layer on the HC surface, whereas ECP method enables kinetically regulated sodium insertion in HC and formation of thinner and more uniform SEI layer on HC surface. These differences strongly influence initial Coulumbic efficiency, interfacial resistance, rate capability, and long-term cycle stability, as demonstrated in Fig. 5d and Fig. S10. The C-rate data (Fig. S10) indicated that the highest capacities were achieved with the DCP cells (red line), where the excess Na^+ ions on the anode surface resulted in a higher capacity, similar to the half-cell performance. However, the DCP and CP (red and blue lines, respectively) cells experienced significant capacity loss during cycling, likely due to side reactions, the formation of inactive residues, and gas release from decomposition reactions [38,41]. By contrast, the ECP cell (green line) showed a superior performance compared with the DCP and CP cells, which could be due to the formation of a more stable SEI layer in the ECP cell [40]. Therefore, while all presodiation strategies present some challenges, further optimization is required for commercialization. Both the DCP and CP methods are more straightforward for practical use than the ECP method because they require specialized procedures during full-cell assembly in a glove box.

Fig. 5e shows the CV curves for the full cells prepared using different

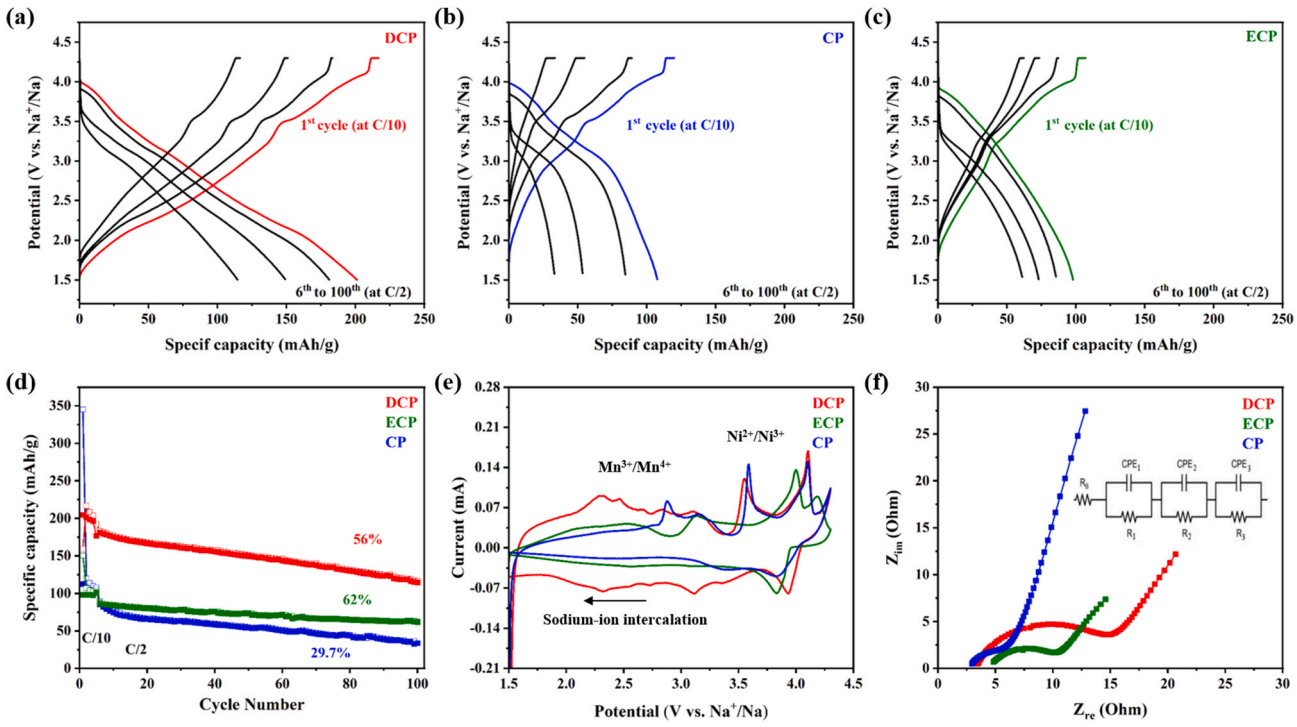

Fig. 5. Galvanostatic performances of full-cell configurations assembled with (a) DCP, (b) CP, and (c) ECP anodes. (d) Capacity retention for 100 cycles at a rate of 0.1 C. Comparison of (e) CV and (f) EIS results along with the EQC model of full cells using DCP, ECP, and CP anodes.

presodiation strategies. The redox mechanism was influenced by the presodiation technique. Three main peaks were identified in the CV data, which are consistent with the CV curves observed in the half-cell configurations (Fig. 2). The primary differences in the DCP (red line), ECP (green line), and CP (blue line) curves are the current values of the Mn^{3+}/Mn^{4+} redox peak. For DCP, the most intense peak was observed at 2.4 V, which reflects the complete reduction of Mn^{4+} to Mn^{3+} throughout the presodiation process during the duration of direct contact. However, this complete reduction was not observed using the ECP and CP presodiation methods. The EIS analyses, along with the equivalent circuit models of these full cells, are shown in Fig. 5f. Model selection is a critical factor for analyzing EIS data, and we used the best-fitting model previously applied to Si-graphite/NMC lithium-ion pouch cells by An et al. [55]. In this model, R_B represents the ohmic resistance, R_1 corresponds to the SEI resistance, R_2 denotes the charge transfer resistance of the cathode, and R_3 refers to the anode charge transfer resistance. The constant phase element (CPE) in the circuit model represents the double-layer capacitive effect. The fitting parameters obtained using the ZMAN software are presented in Table S4. The R_B values for the full cells using CP (2.71 Ω), DCP (4.47 Ω), and ECP (3.31 Ω) methods were similar, reflecting internal resistances from the various components, such as the current collector, electrolyte, and separator. R_1, which is important for evaluating the SEI layer, was the lowest for the DCP (64.6 Ω) method compared to ECP (361 Ω) and CP (100 Ω), which corresponded to the highest initial capacity among all methods. Because the cathodes were the same in all three cells, the R_2 values were expected to be similar [41]. The R_3 value associated with the anode is influenced by the sodium content introduced through presodiation. The lowest R_3 value was observed for the ECP method (0.873 Ω), suggesting a fast Na^+ diffusion during electrochemical cycling. By contrast, the CP- and DCP-based full-cells showed high R_3 values (216 and 76.7 Ω, respectively), confirming fast capacity decay during cycling; however, the DCP method offered advantages regarding D_{Na+} in the anode compared to the CP method. Therefore, we assert that R_3 is an important parameter affecting battery performance during the presodiation process. Overall, this study shows that SEI formation through presodiation strategies is a critical factor affecting stable cell production. Different methods for SEI formation involve various factors that influence battery performance. An unstable SEI or its decomposition significantly affects the cyclability of cells. However, these limitations can be overcome using the DCP method, although further experimentation and evaluation are required to achieve improved cycling stability. Although the study demonstrates promising results for presodiated HC anodes in SIBs, the scalability and long-term stability of the presodiation methods require further investigation.

3. Conclusions

This paper presents an in-depth investigation into the development of cost-effective SIBs using P2-$Na_{0.67}Ni_{0.1}Mn_{0.9}O_2$ and lavender-flower-waste-derived HC as the cathode and anode, respectively. Comprehensive analyses of $Na_{0.67}Ni_{0.1}Mn_{0.9}O_2$ and HC using SEM, TEM, XPS, XRD, XAS, RAMAN, and FTIR confirmed the elemental composition, surface chemistry, structural integrity, and redox reactions involving Mn^{3+}/Mn^{4+} and Ni^{2+}/Ni^{3+}. Three different presodiation strategies were investigated, and the ECP method proved to be the most effective, delivering a 62 % capacity retention after 100 cycles, compared to the CP (29.7 %) and DCP (56 %) methods, where the formation and stability of the SEI layer play a significant role in the long-term cycling performance of full cells. This comprehensive study highlights the potential for developing SIBs with low-cost and sustainable electrode materials. The optimization of presodiation strategies offers an opportunity for advanced commercial and scalable SIB technologies.

4. Experimental section

4.1. Materials and methods

4.1.1. Synthesis of $Na_{0.67}Ni_{0.10}Mn_{0.90}O_2$ cathodes

To synthesize the $Na_{0.67}Ni_{0.10}Mn_{0.90}O_2$ cathode powders, sodium peroxide (Na_2O_2), manganese (III) oxide (Mn_2O_3), and nickel (II) oxide (NiO) were thoroughly mixed for 1 h in an agate mortar. This step is

necessary to ensure homogeneity. A pressure of 100 bar was applied to press the powder mixture into pellets. The samples were heated in a high-temperature furnace to 900 °C for 4 h in air at a heating rate of 10 °C/min. After 4 h, the pellets were quenched in liquid nitrogen (LN_2) to obtain the desired crystalline structures. The samples were stored in a glovebox.

4.1.2. Synthesis of HC anodes

Lavender flowers purchased from a local market in Türkiye were dried in air at 24 °C for one month. The dried flowers were ground and exposed to heat treatment at 1300 °C for 4 h with 10 °C/min heating and cooling rates under a high-purity argon gas flow. The resulting powder was soaked in a 0.1 M hydrochloric acid (HCl) solution for 6 h to facilitate demineralization. The undesired inorganic components were removed by repeatedly washing the powder with deionized water until the pH of the solution reached 7.0, ensuring complete removal of HCl.

4.2. Material characterization

4.2.1. Structural characterization

The surface composition and oxidation states of the elements in the samples were studied using XPS, in which the spectra were calibrated using the C1s standard at 284.8 eV. Rietveld refinement with the GSAS-II software was used to calculate the cell parameters. The combination of these techniques yielded a comprehensive understanding of the structural and compositional properties of the powders. Brunauer–Emmett–Teller (BET) measurements were performed using Micrometrics Gemini VII Version 3.03 to determine the surface area. X-ray absorption near-edge structure (XANES) and extended XAFS (EXAFS) measurements were conducted at the BM08-XAFS/XRF beamline at Synchrotron-light for Experimental Science and Applications in the Middle East (SESAME), Jordan. Mn and Ni K-edge data were collected in the fluorescence mode while the cells cycled between 1.5 and 4.3 V at a 30 mA/g. The collected data were processed using the DeMeter and WunXAS software packages. Time-of-flight secondary ion mass spectroscopy (TOF-SIMS) was performed using an ION-TOF instrument (Münster, Germany) under an ultrahigh vacuum ($<2 \times 10^{-9}$ mbar). The spectral and depth profiles of the samples were obtained using a pulsed 30-keV Bi^{3+} ion beam. The cathode was sputtered with a 3-keV Cs^{+} ion beam. An FEI Titan TM 80–300 microscope (at 30 kV) was used to obtain high-angle annular dark-field transmission electron microscopy (HAADF-TEM), scanning transmission electron microscopy (STEM), and high-resolution transmission electron microscopy (HR-TEM) images and to collect selected area diffraction (SAED) patterns. In situ XRD measurements were conducted using a time-resolved X-ray diffractometer (TR-XRD) between 10 and 90° with 180 s data collection intervals for each scan at the Korea Institute of Science and Technology in South Korea.

4.2.2. Theoretical characterization

The electronic properties of $Na_{0.67}MnO_2$ and $Na_{0.67}Ni_{0.1}Mn_{0.9}O_2$ were determined by DFT calculations using the Vienna Ab initio Simulation Package. To expand the Kohn–Sham orbitals and build pseudopotentials, the projector augmented-wave method was used with a cutoff energy of 37 Ry. The Gaussian smearing factor for the Fermi level was 0.03 eV. The accuracy of the total energies was set to 10^{-6} eV. The initial structure of $Na_{0.67}MnO_2$ was obtained by Rietveld refinement.

4.2.3. Electrochemical characterization

The half-cell electrochemical properties of the electrodes were studied in CR2032 coin cells using sodium metal as the counter electrode. To obtain a slurry, the active material, supercarbon, and polyvinylidene fluoride binder were mixed at weight ratios of 80:10:10 and 70:20:10 for the anode and cathode, respectively. Magnetic stirring and ultrasonic homogenization were applied to obtain homogenous mixtures. The slurry was coated on aluminum foil using a doctor blade. A vacuum oven was used to dry the electrodes at 110 °C for 24 h, and 15-mm discs were then cut from the electrodes. The CR2032 coin cells were assembled using Whatman GF/B separators. Sodium perchlorate ($NaClO_4$, 1 M) dissolved in a 50:50 (v/v) mixture of ethylene carbonate and propylene carbonate, was used as the electrolyte. Cyclic voltammetry (CV), electrochemical impedance spectroscopy (EIS), galvanostatic intermittent titration technique (GITT), and galvanostatic cycling tests were conducted to study the electrochemical properties. The scan rate for the CV measurements was 0.1 mV/s within voltage windows of 1.5–4.3 V and 0.0–3.0 V for the cathode and anode, respectively. EIS analysis provided insights into the charge transfer resistance and overall cell impedance using a 10 mV AC signal over a frequency range of 1 mHz–200 kHz. Galvanostatic cycling measurements were performed over 100 cycles at C/3 and 30 mA/g for the cathode and anode, respectively. In the full-cell assembly, we employed three different presodiation strategies (**Note S1**) for the anode: (i) direct-contact presodiation (DCP), (ii) electrochemical cycling presodiation (ECP), and (iii) chemical presodiation (CP). The electrochemical properties of these full cells were evaluated using a similar characterization to that of the half-cell configuration, including EIS, CV, cycling performance, and C-rate measurements.

CRediT authorship contribution statement

Ebru Dogan: Investigation, Formal analysis. **Iqra Moeez:** Writing – review & editing, Writing – original draft, Methodology, Investigation, Formal analysis, Data curation. **Rawdah Whba:** Writing – review & editing, Investigation, Formal analysis, Conceptualization. **Sibel Ozcan:** Investigation, Formal analysis, Conceptualization. **Mitat Akkoc:** Investigation, Conceptualization. **Emine Altin:** Visualization, Investigation, Formal analysis, Conceptualization. **Messaoud Harfouche:** Visualization, Investigation, Formal analysis, Conceptualization. **Aydin Aktas:** Visualization, Investigation. **Fatih Bulut:** Investigation, Data curation. **Muhammad Arshad:** Formal analysis, Conceptualization. **Ismail Ozdemir:** Writing – review & editing, Investigation. **Saban Patat:** Writing – original draft, Investigation. **Kyung Yoon Chung:** Writing – review & editing, Supervision, Project administration, Investigation, Funding acquisition, Data curation, Conceptualization. **Sevda Sahinbay:** Writing – review & editing, Writing – original draft, Visualization, Methodology, Investigation, Formal analysis, Conceptualization. **Serdar Altin:** Writing – review & editing, Writing – original draft, Visualization, Resources, Project administration.

Declaration of competing interest

The authors declare that they have no known competing financial interests or personal relationships that could have appeared to influence the work reported in this paper.

Acknowledgements

The authors acknowledge the financial support of Inonu University under project number FDP-2024-3694. The Operando XAFS analysis was performed at BM08-XAFS/XRF Beamline in SESAME, Jordan, and TENMAK financially supported the authors during the experiment in SESAME. The work done at KIST was supported by the National Research Foundation of Korea (RS-2024-00404414) funded by the Ministry of Science and ICT, the National Research Council of Science & Technology(NST) grant by the Korea government (MSIT) (No. GTL24011-000), and the KIST Institutional Program (Project No. 2E33940).

Appendix A. Supplementary data

Supplementary data to this article can be found online at https://doi.org/10.1016/j.jpowsour.2026.239365.

Data availability

Data will be made available on request.

References

[1] M.G.M. Abdolrasol, S. Ansari, I.A. Sarker, S.K. Tiong, M.A. Hannan, Lithium-ion to sodium-ion batteries transitioning: trends, analysis and innovative technologies prospects in EV application, Prog. Energy 7 (2025), https://doi.org/10.1088/2516-1083/ADBFF0.

[2] A.J. Jannesar Niri, G.A. Poelzer, S.E. Zhang, J. Rosenkranz, M. Pettersson, Y. Ghorbani, Sustainability challenges throughout the electric vehicle battery value chain, Renew. Sustain. Energy Rev. 191 (2024) 114176, https://doi.org/10.1016/J.RSER.2023.114176.

[3] M. He, S. Liu, J. Wu, J. Zhu, Review of cathode materials for sodium-ion batteries, Prog. Solid State Chem. 74 (2024) 100452, https://doi.org/10.1016/J.PROGSOLIDSTCHEM.2024.100452.

[4] J.Y. Hwang, S.T. Myung, Y.K. Sun, Sodium-ion batteries: present and future, Chem. Soc. Rev. 46 (2017) 3529–3614, https://doi.org/10.1039/c6cs00776g.

[5] Y. Wu, W. Shuang, Y. Wang, F. Chen, S. Tang, X.L. Wu, Z. Bai, L. Yang, J. Zhang, Recent progress in sodium-ion batteries: advanced materials, reaction mechanisms and energy applications, Electrochem. Energy Rev. 7 (2024) 1–50, https://doi.org/10.1007/S41918-024-00215-Y.

[6] L. Sun, J. Zeng, X. Wan, Chenxi Peng, J. Wang, C. Lin, M. Zhu, J. Liu, Recent progress of interface modification of layered oxide cathode material for sodium-ion batteries, Electron 2 (2024) e31, https://doi.org/10.1002/ELT2.31.

[7] Y. Gupta, P. Siwatch, R. Karwasra, K. Sharma, S.K. Tripathi, Recent progress of layered structured P2- and O3- type transition metal oxides as cathode material for sodium-ion batteries, Renew. Sustain. Energy Rev. 192 (2024) 114167, https://doi.org/10.1016/J.RSER.2023.114167.

[8] L. Li, Y. Zheng, S. Zhang, J. Yang, Z. Shao, Z. Guo, Recent progress on sodium ion batteries: potential high-performance anodes, Energy Environ. Sci. 11 (2018) 2310–2340, https://doi.org/10.1039/C8EE01023D.

[9] R.J. Clément, P.G. Bruce, C.P. Grey, J. Review—manganese-based P2-Type transition metal oxides as sodium-ion battery cathode materials, Electrochem. Soc. 162 (2015) A2589–A2604, https://doi.org/10.1149/2.0201514jes.

[10] Z. Lu, J.R. Dahn, In situ X-Ray diffraction study of P2-$Na_{2/3}Ni_{1/3}Mn_{2/3}O_2$, J. Electrochem. Soc. 148 (2001) A1225, https://doi.org/10.1149/1.1407247.

[11] N. Yabuuchi, M. Kajiyama, J. Iwatate, H. Nishikawa, S. Hitomi, R. Okuyama, R. Usui, Y. Yamada, S. Komaba, P2-Type $Na_xFe_{1/2}Mn_{1/2}O_2$ made from earth-abundant elements for rechargeable Na^+ batteries, Nat. Mater. 11 (2012) 512–517, https://doi.org/10.1038/nmat3309.

[12] J. Xu, S.-L. Chou, J.-L. Wang, H.-K. Liu, S.-X. Dou, Layered P2-$Na_{0.66}Fe_{0.5}Mn_{0.5}O_2$ cathode material for rechargeable sodium-ion batteries, Chemelectrochem 1 (2014) 371–374, https://doi.org/10.1002/celc.201300026.

[13] J. Yoshida, E. Guerin, M. Arnault, C. Constantin, B.M. Mortemard de Boisse, D. Carlier, M. Guignard, C. Delmas, New P2-$Na_{0.70}Mn_{0.60}Ni_{0.30}Co_{0.10}O_2$ layered oxide as electrode material for Na-Ion batteries, J. Electrochem. Soc. 161 (2014) A1987–A1991, https://doi.org/10.1149/2.0121414JES.

[14] M. Le Nguyen, H. Van Nguyen, N. Ghosh, A. Garg, M. Van Tran, P.M.L. Le, High-voltage performance of P2-$Na_xMn_{0.5}Co_{0.5}O_2$ layered cathode material, Int. J. Energy Res. 4 (2022) 5119–5133, https://doi.org/10.1002/ER.7504.

[15] P. Hou, M. Dong, Z. Lin, Z. Sun, M. Gong, F. Li, X. Xu, Alleviating the jahn-teller distortion of P3-Type manganese-based cathodes by compositionally graded structure for sodium-ion batteries, ACS Sustainable Chem. Eng. 11 (2023) 10785–10794, https://doi.org/10.1021/ACSSUSCHEMENG.3C01854/SUPPL_FILE/SC3C01854_SI_001.PDF.

[16] L. Zheng, Z. Wang, M. Wu, B. Xu, C. Ouyang, Jahn–teller type small polaron assisted Na diffusion in NaMnO2 as a cathode material for Na-Ion batteries, J. Mater. Chem. A 7 (2019) 6053–6061, https://doi.org/10.1039/C8TA11955D.

[17] R. Liu, C.H. Shen, Structural and electrochemical study of cobalt doped $LiMn_2O_4$ spinels, Solid State Ionics 157 (2003) 95–100, https://doi.org/10.1016/S0167-2738(02)00194-7.

[18] X. Zhang, F. Qiu, K. Jiang, P. He, M. Han, S. Guo, H. Zhou, Improving the structural and cyclic stabilities of P2-Type $Na_{0.67}MnO_2$ cathode material via Cu and Ti Co-Substitution for sodium ion batteries, Chem. Commun. 56 (2020) 6293–6296, https://doi.org/10.1039/D0CC01442G.

[19] R. Luo, J. Zheng, Z. Zhou, J. Li, Y. Li, Z. He, Study of synergistic effects of Cu and Fe on P2-Type $Na_{0.67}MnO_2$ for high performance Na-Ion batteries, ACS Appl. Mater. Interfaces 14 (2022) 47863–47871, https://doi.org/10.1021/acsami.2c12894.

[20] B. Kalyoncuoglu, M. Ozgul, S. Altundag, E. Altin, I. Moeez, K.Y. Chung, M. Arshad, M.G. Aydin, T. Depci, S. Altin, S. Sahinbay, High-performance Ag-Doped $Na_{0.67}MnO_2$ cathode: Operando XRD study and full-cell performance analysis with presodiated anode, ACS Appl. Energy Mater. 6 (2023) 11993–12002, https://doi.org/10.1021/acsaem.3c02134.

[21] G.K. Wazny, K. Walczak, J. Tobola, M. Rybski, W. Zając, P. Czaja, M. Wolczko, J. Płotek, J. Molenda, Effect of Mg substitution on structural stabilization of Na_xMnO_2 cathode for Na-Ion batteries, Energy Technol. 11 (2023) 2300139, https://doi.org/10.1002/ENTE.202300139.

[22] X. Liu, W. Zuo, B. Zheng, Y. Xiang, K. Zhou, Z. Xiao, P. Shan, J. Shi, Q. Li, G. Zhong, R. Fu, Y. Yang, P2-$Na_{0.67}Al_xMn_{1-x}O_2$: cost-effective, stable and high-rate sodium electrodes by suppressing phase transitions and enhancing sodium cation mobility, Angew Chem. Int. Ed. Engl. 58 (2019) 18086–18095, https://doi.org/10.1002/ANIE.201911698.

[23] Q. Ding, W. Zheng, A. Zhao, Y. Zhao, K. Chen, X. Zhou, H. Zhang, W-Doping induced efficient tunnel-to-layered structure transformation of $Na_{0.44}Mn_{1-x}W_xO_2$: phase evolution , sodium-storage properties , and moisture stability, Adv. Energy Mater. 13 (2023) 2203802, https://doi.org/10.1002/aenm.202203802.

[24] Y.-Y. Zhang, S.-J. Zhang, J.-T. Li, K. Wang, Y.-C. Zhang, Q. Liu, R.-S. Xie, Y.-R. Pei, L. Huang, S.-G. Sun, Improvement of electrochemical properties of P2-Type $Na_{2/3}Mn_{2/3}Ni_{1/3}O_2$ sodium ion battery cathode material by water-soluble binders, Electrochim. Acta 298 (2019) 496–504, https://doi.org/10.1016/J.ELECTACTA.2018.12.089.

[25] C. Ma, J. Alvarado, J. Xu, R.J. Clément, M. Kodur, W. Tong, C.P. Grey, Y.S. Meng, Exploring oxygen activity in the high energy P2-Type $Na_{0.78}Ni_{0.23}Mn_{0.69}O_2$ cathode material for Na-Ion batteries, J. Am. Chem. Soc. 139 (2017) 4835–4845, https://doi.org/10.1021/JACS.7B00164.

[26] B. Peng, Z. Sun, S. Jiao, G. Wang, G. Zhang, Electrochemical performance optimization of layered P2-Type $Na_{0.67}MnO_2$ through simultaneous Mn-Site doping and nanostructure engineering, Batter. Supercaps 3 (2020) 147–154, https://doi.org/10.1002/BATT.201900126.

[27] Q. Xiao, Z. Guo, J. Huang, S. Zhong, Effects of the Mn/Ni ratio on the battery performance of layered na-ni-mn oxide cathode materials in sodium-ion batteries, Ionics 30 (2024) 207–216, https://doi.org/10.1007/s11581-023-05277-4.

[28] V. Simone, A. Boulineau, A. de Geyer, D. Rouchon, L. Simonin, S. Martinet, Hard carbon derived from cellulose as anode for sodium ion batteries: dependence of electrochemical properties on structure, J. Energy Chem. 25 (2016) 761–768, https://doi.org/10.1016/J.JECHEM.2016.04.016.

[29] J. Yin, Y.S. Zhang, H. Liang, W. Zhang, Y. Zhu, Synthesis strategies of hard carbon anodes for sodium-ion batteries, Mater. Rep. Energy 4 (2024) 100268, https://doi.org/10.1016/J.MATRE.2024.100268.

[30] X. Chen, N. Sawut, K. Chen, H. Li, J. Zhang, Z. Wang, Filling carbon: a microstructure-engineered hard carbon for efficient alkali metal ion storage, Energy Environ. Sci. 16 (2023) 4041–4053, https://doi.org/10.1039/d3ee01154b.

[31] Q. Zhang, X. Deng, M. Ji, Y. Li, Z. Shi, Hard carbon microspheres derived from resorcinol formaldehyde resin as high-performance anode materials for sodium-ion battery, Ionics 26 (2020) 4523–4532, https://doi.org/10.1007/s11581-020-03585-7.

[32] L. Rakhymbay, N. Bazybek, K. Kudaibergenov, S.T. Myung, Z. Bakenov, A. Konarov, Present development and future perspectives on biowaste-derived hard carbon anodes for room temperature sodium-ion batteries, J. Power Sources 602 (2024) 234347, https://doi.org/10.1016/J.JPOWSOUR.2024.234347.

[33] M. Thenappan, S. Rengapillai, S. Marimuthu, Hard carbon reprising porous morphology derived from coconut sheath for sodium-ion battery, Energies 15 (2022) 8086, https://doi.org/10.3390/EN15218086.

[34] C. Wang, D. Sen, V.K. Aswal, L. Weiguang, P. Balaya, Enhanced storage performance of a low-cost hard carbon derived from biomass, Carbon Trends 17 (2024) 100415, https://doi.org/10.1016/J.CARTRE.2024.100415.

[35] F.N. Shafiee, S.A. Mohd Noor, M.A.A. Mohd Abdah, S.H. Jamal, A. Samsuri, Recent progress on hard carbon and other anode materials for sodium-ion batteries, Heliyon 10 (2024) e29512, https://doi.org/10.1016/J.HELIYON.2024.E29512.

[36] D. Alvira, D. Antorán, J.J. Manyà, Plant-derived hard carbon as anode for sodium-ion batteries: a comprehensive review to guide interdisciplinary research, Chem. Eng. J. 447 (2022), https://doi.org/10.1016/j.cej.2022.137468.

[37] B. Pakdemirli, Economic importance of medicinal and aromatic plants in Turkey: the examples of thyme and lavender, Bahçe 49 (2020) 51–58.

[38] I. Moeez, H.G. Jung, H.D. Lim, K.Y. Chung, Presodiation strategies and their effect on electrode-electrolyte interphases for high-performance electrodes for sodium-ion batteries, ACS Appl. Mater. Interfaces 11 (2019) 41394–41401, https://doi.org/10.1021/acsami.9b14381.

[39] E. Dogan, R. Whba, E. Altin, I. Moeez, K.Y. Chung, R. Stoyanova, V. Koleva, A. Aktas, S. Altin, S. Sahinbay, Optimized performance of $Na_{0.67}Mn_{0.5}Fe_{0.5}O_2$@ TiO_2 and presodiated hard carbon (Pre-SHC) full-cells using direct contact method, J. Power Sources 632 (2025) 236327, https://doi.org/10.1016/j.jpowsour.2025.236327.

[40] G. Sun, G. Wu, P. Ding, Y. Yang, Z. Wang, J. Xu, X. Wu, Constructing all-climate hybrid sodium Ion/metal batteries through intersolvent synergistic effect, ACS Energy Lett. 10 (2025) 3315–3324, https://doi.org/10.1021/acsenergylett.5c01080.

[41] M. Liu, J. Zhang, S. Guo, B. Wang, Y. Shen, X. Ai, H. Yang, J. Qian, Chemically presodiated hard carbon anodes with enhanced initial coulombic efficiencies for high-energy sodium ion batteries, ACS Appl. Mater. Interfaces 12 (2020) 17620–17627, https://doi.org/10.1021/acsami.0c02230.

[42] Z. Liu, J. Liu, J. Structural, Evolution in P2-Type layered oxide cathode materials for sodium-ion batteries, ChemNanoMat 8 (2022) e202100385, https://doi.org/10.1002/CNMA.202100385.

[43] S. Chen, E. Han, H. Xu, L. Zhu, B. Liu, G. Zhang, M. Lu, P2-Type $Na_{0.67}Ni_{0.33-x}Cu_xMn_{0.67}O_2$ as new high-voltage cathode materials for sodium-ion batteries, Ionics 23 (2017) 3057–3066, https://doi.org/10.1007/s11581-017-2122-x.

[44] B. Kalyoncuoglu, M. Ozgul, S. Altundag, F. Bulut, E. Oz, S. Sahinbay, S. Altin, High-performance Na-Ion full-cells with P2-Type $Na_{0.67}Mn_{0.5-x}Ni_xFe_{0.43}Al_{0.07}O_2$ cathodes: cost analysis for stationary battery storage systems, J. Energy Storage 79 (2024) 110203, https://doi.org/10.1016/J.EST.2023.110203.

[45] M. Venkatesh, G.S. Priyanga, S. Sharma, P.L.M. Kanta, T. Thomas, R. Gopalan, B. Das, Effect of dopants and microstructure on the electrochemical cyclic stability of layered P2-Type $Na_{0.67}MnO_2$ prepared by different chemical routes: an experimental and theoretical study, Ceram. Int. 49 (2023) 6654–6665, https://doi.org/10.1016/J.CERAMINT.2022.11.002.

[46] S.L. Dudarev, G.A. Botton, S.Y. Savrasov, C.J. Humphreys, A.P. Sutton, Electron-energy-loss spectra and the structural stability of nickel oxide: an LSDA+U study, Phys. Rev. B 57 (1998) 1505–1509, https://doi.org/10.1103/PhysRevB.57.1505.

[47] J.P. Perdew, K. Burke, M. Ernzerhof, Generalized gradient approximation made simple, Phys. Rev. Lett. 77 (1996) 3865–3868, https://doi.org/10.1103/PhysRevLett.77.3865.

[48] B. Li, R. Shao, H. Yan, L. An, B. Zhang, H. Wei, J. Ma, D. Xia, X. Han, Understanding the stability for Li-Rich layered oxide Li_2RuO_3 cathode, Adv. Funct. Mater. 26 (2016) 1330–1337, https://doi.org/10.1002/ADFM.201504836.

[49] M. Giot, L.C. Chapon, J. Androulakis, M.A. Green, P.G. Radaelli, A. Lappas, Magnetoelastic coupling and symmetry breaking in the frustrated antiferromagnet α-$NaMnO_2$, Phys. Rev. Lett. 99 (2007) 247211, https://doi.org/10.1103/PhysRevLett.99.247211.

[50] Z.M. Oktay, Y. Onal, T. Depci, S. Altundag, S. Altin, S. Yaşar, E. Altin, Investigation of electrochemical performance of Na-Ion batteries by hard carbon anodes produced by biomass of Prunus Armeniaca seeds, J. Mater. Sci. Mater. Electron. 34 (2023) 1–12, https://doi.org/10.1007/S10854-023-10849-1/FIGURES/9.

[51] J. Mei, T. Wang, D. Qi, J. Liu, T. Liao, Y. Yamauchi, Z. Sun, Three-dimensional fast Na-Ion transport in sodium titanate nanoarchitectures via engineering of oxygen vacancies and bismuth substitution, ACS Nano 15 (2021) 13604–13615, https://doi.org/10.1021/acsnano.1c04479.

[52] I. Moeez, D. Susanto, G. Ali, H.G. Jung, H.D. Lim, K.Y. Chung, Effect of the interfacial protective layer on the NaFe0.5Ni0.5O2cathode for rechargeable sodium-ion batteries, J. Mater. Chem. A 8 (2020) 13964–13970, https://doi.org/10.1039/D0TA02837A.

[53] X. Ding, C. Jiang, Y. Fan, Y. Yang, L. Liu, Y. Xiao, L. Han, Slope-structure design towards high-stability P2-$Na_{0.67}MnO_2$ cathode, Chem. Eng. J. 499 (2024) 156294, https://doi.org/10.1016/J.CEJ.2024.156294.

[54] C. Yang, J. Wang, C. Sang, W. Zheng, H. Cui, X. Ai, Y. Cao, Y. Fang, In situ engineering of a multifunctional cathode–electrolyte interphase for advanced sodium-ion batteries, ACS Energy Lett. 10 (2025) 3544–3553, https://doi.org/10.1021/acsenergylett.5c01335.

[55] S.J. An, J. Li, C. Daniel, H.M. Meyer, S.E. Trask, B.J. Polzin, D.L. Wood, Electrolyte volume effects on electrochemical performance and solid electrolyte interphase in Si-Graphite/NMC lithium-ion pouch cells, ACS Appl. Mater. Interfaces 9 (2017) 18799–18808, https://doi.org/10.1021/acsami.7b03617.